ADVANCED ENERGY MATERIALS
www.advenergymat.de

Aqueous MXene/PH1000 Hybrid Inks for Inkjet-Printing Micro-Supercapacitors with Unprecedented Volumetric Capacitance and Modular Self-Powered Microelectronics

Jiaxin Ma, Shuanghao Zheng, Yuexian Cao, Yuanyuan Zhu, Pratteek Das, Hui Wang, Yu Liu, Jiemin Wang, Liping Chi, Shengzhong (Frank) Liu, and Zhong-Shuai Wu**

Despite intense development of inkjet printing for scalable and customizable fabrication of power sources, one major shortcoming is the lack of eco-friendly aqueous inks free of additives (e.g., toxic solvents, surfactants). Here, an aqueous printable MXene/poly(3,4-ethylenedioxythiophene):poly(styrenesulfonic acid) (MP) hybrid ink is demonstrated that has an adjustable viscosity to directly inkjet-print micro-supercapacitors (MP-MSCs) with excellent performance, seamless integration, and desirable customization, which is crucial for scalable industrialization of self-powered integrated systems. The MP-MSCs deliver an unprecedented volumetric capacitance of 754 F cm^{-3} and a remarkable energy density of 9.4 mWh cm^{-3}, superior to previously reported inkjet-printed MSCs. Such outstanding performance is partly attributed to highly conductive PH1000 that prevents restacking of MXene nanosheets, enabling fast electron and ion diffusion throughout the microelectrodes. Moreover, MP-MSCs present exceptional miniaturization and superior modularization featuring high voltage output up to 36 V from 60 serially connected cells and impressive areal voltage of 5.4 V cm^{-2} connected in tandem. Further, a printable temperature sensor integrated with the MP-MSC and a flexible solar cell exhibits an exceptional response of 2% and mechanical flexibility without any bias voltage input. Therefore, the MXene inks are expected to create various opportunities for miniaturization and innovative construction of flexible, self-sustaining, energy harvesting–storing–consuming microsystems for printable electronics.

1. Introduction

The development of digital technology has reached the point where the demands on portable and flexible microscale electrochemical energy storage devices (MEESDs) have gone beyond simply achieving high performance to include the incorporation of customizable shape, flexibility, and seamless integration with microelectronics.[1–7] Integration of MEESDs with microelectronics can solve an array of problems associated with traditional MEESDs by allowing the conversion of intermittent renewable energy sources (e.g., solar, water, thermal, and mechanical energy) into a usable form through portable systems, hence saving additional power and cost.[8–13] The examples of a self-charging electrochromic microsupercapacitor (MSC) integrated with the hybrid tribo/piezoelectric nanogenerators powering a light emitting diode,[14] and a stretchable integrated system composed of a MSC, solar cells, and a strain sensor monitoring arterial pulse[15] show glimpses of a future where energy is harvested and used "on-the-go" without time lag. However, the current microsystems mostly

J. Ma, Dr. S. Zheng, Dr. Y. Zhu, P. Das, Y. Liu, Dr. J. Wang, L. Chi, Prof. Z.-S. Wu
State Key Laboratory of Catalysis
Dalian Institute of Chemical Physics
Chinese Academy of Sciences
457 Zhongshan Road, Dalian 116023, China
E-mail: wuzs@dicp.ac.cn

J. Ma, P. Das
University of Chinese Academy of Sciences
19 A Yuquan Road, Shijingshan District, Beijing 100049, China

Dr. S. Zheng, Dr. Y. Cao, Prof. H. Wang, Prof. S. (F.) Liu, Prof. Z.-S. Wu
Dalian National Laboratory for Clean Energy
Chinese Academy of Sciences
457 Zhongshan Road, Dalian 116023, China
E-mail: szliu@dicp.ac.cn

L. Chi
College of Materials Science and Engineering
Dalian Jiaotong University
794 Huanghe Road, Dalian 116028, China

Prof. S. (F.) Liu
Key Laboratory of Applied Surface and Colloid Chemistry
Ministry of Education
Shaanxi Key Laboratory for Advanced Energy Devices
Shaanxi Engineering Lab for Advanced Energy Technology
School of Materials Science and Engineering
Shaanxi Normal University
620 West Chang'an Street, Xi'an 710119, China

The ORCID identification number(s) for the author(s) of this article can be found under https://doi.org/10.1002/aenm.202100746.

DOI: 10.1002/aenm.202100746

depend on costly and complex fabrication techniques, such as laser carving and photolithography that are incompatible with the mass production of microelectronics.[16,17] Alternatively, printing techniques (e.g., screen printing, inkjet printing, 3D printing, and spray printing) are receiving widespread attention, mainly as they are scalable and allow fabrication of shape-diverse microdevices seamlessly integrated to provide tailored performance.[18–22] Among these printing methods, inkjet printing is a high-precision, non-contact, and fully additive process that does not require masks for patterning; thus, it is deemed a promising strategy for the customizable design of smart and flexible electronics.[23–25] The challenge now lies in the controllable synthesis of corresponding inks that overcome typical problems like nonstability and poor printability while being non-toxic.[26]

MXene, especially $Ti_3C_2T_x$ (T_x represents the surface terminations), exhibits ultrahigh electrical conductivity (≈9800 S cm^{-1}) and volumetric capacitance (≈1500 F cm^{-3}), and unique mechanical and optical properties.[27–30] In particular, with an abundance of functional groups (e.g., −F, −OH, −O) on the surface, it is possible to fabricate stable MXene inks with high dispersibility.[31–34] For example, Zhang et al. prepared a pure MXene ink in *N*-methyl-2-pyrrolidone (NMP) and dimethylformamide (DMF) by a solvent exchange approach.[35] The printed MXene ink with suitable viscosity and surface tension was stably extruded from the nozzle to construct flexible MSCs with high precision. However, the printed MXene microelectrodes with layered $Ti_3C_2T_x$ flakes often got restacked, hence impeding ionic diffusion and resulting in low areal (<12 mF cm^{-2}) and volumetric (<600 F cm^{-3}) capacitance. Moreover, the involved toxic solvents, e.g., DMF and NMP, of the MXene inks were not environmentally friendly, which greatly limited the prospects for large-scale production. Hence, it is desirable to exploit a nontoxic aqueous MXene ink to alleviate the restacking issue as well as improve electrochemical performance. It is worth noting that PH1000 with excellent aqueous solution processibility and specific chain structure easily attached to the surface of MXene to avoid the restacking of MXene nanosheets,[36] thereby it would be a good choice as a conductive filler for MXene ink.

Herein, we report an aqueous MXene/PH1000 (MP) hybrid ink for customizable fabrication of planar MSCs with excellent shape diversity, record volumetric capacitance, exceptional integration, and modularization capabilities. This ink is rationally designed to offer high conductivity, adjustable viscosity, remarkable printability, and long-term stability, all contributing to the fabrication of electrochemically and mechanically robust microelectrodes. The resulting MP-MSCs delivered an outstanding volumetric capacitance (754 F cm^{-3}) and a satisfactory energy density (9.4 mWh cm^{-3}), higher than those of most inkjet-printed MSCs. This is attributed to the role of PH1000 in enhancing interlayer contact in the MXene to greatly promoted electron and ion transfer. To further meet the demand for an integrated planar power system, we connected our MSCs with a flexible solar cell to charge a self-powered temperature sensor (TS). The exceptional response of ≈2% is a notably high efficiency, demonstrative of the successful integration.

2. Results and Discussion

2.1. Fabrication of MSCs and Self-Powered Integrated System

The printing and assembly processes of the MP ink for MSCs as well as the self-powered TS are schematically presented in **Figure 1**. The aqueous MP ink consisted of MXene and PH1000 with excellent solution processibility, suitable viscosity, and surface energy well-matched with the substrates. Thus, the MP ink

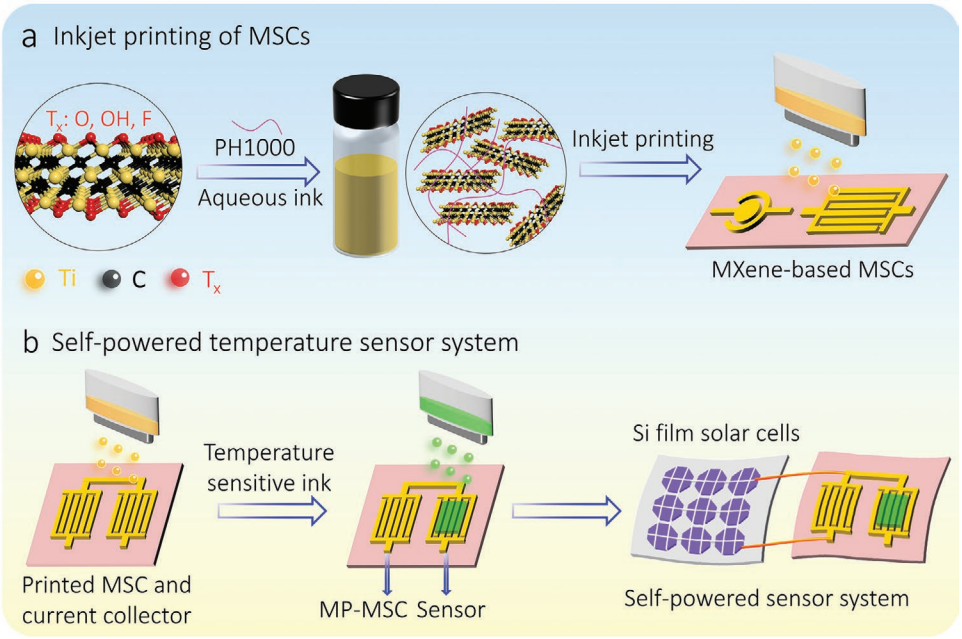

Figure 1. Schematic illustration of the fabrication of inkjet-printed MP-MSCs and the self-powered integrated system. a) Schematic of the aqueous MP hybrid ink for inkjet printing MP-MSCs. b) Construction of the self-powered temperature sensor system by inkjet-printing a MP-MSC and a temperature sensor and connecting a Si film solar cell via wires.

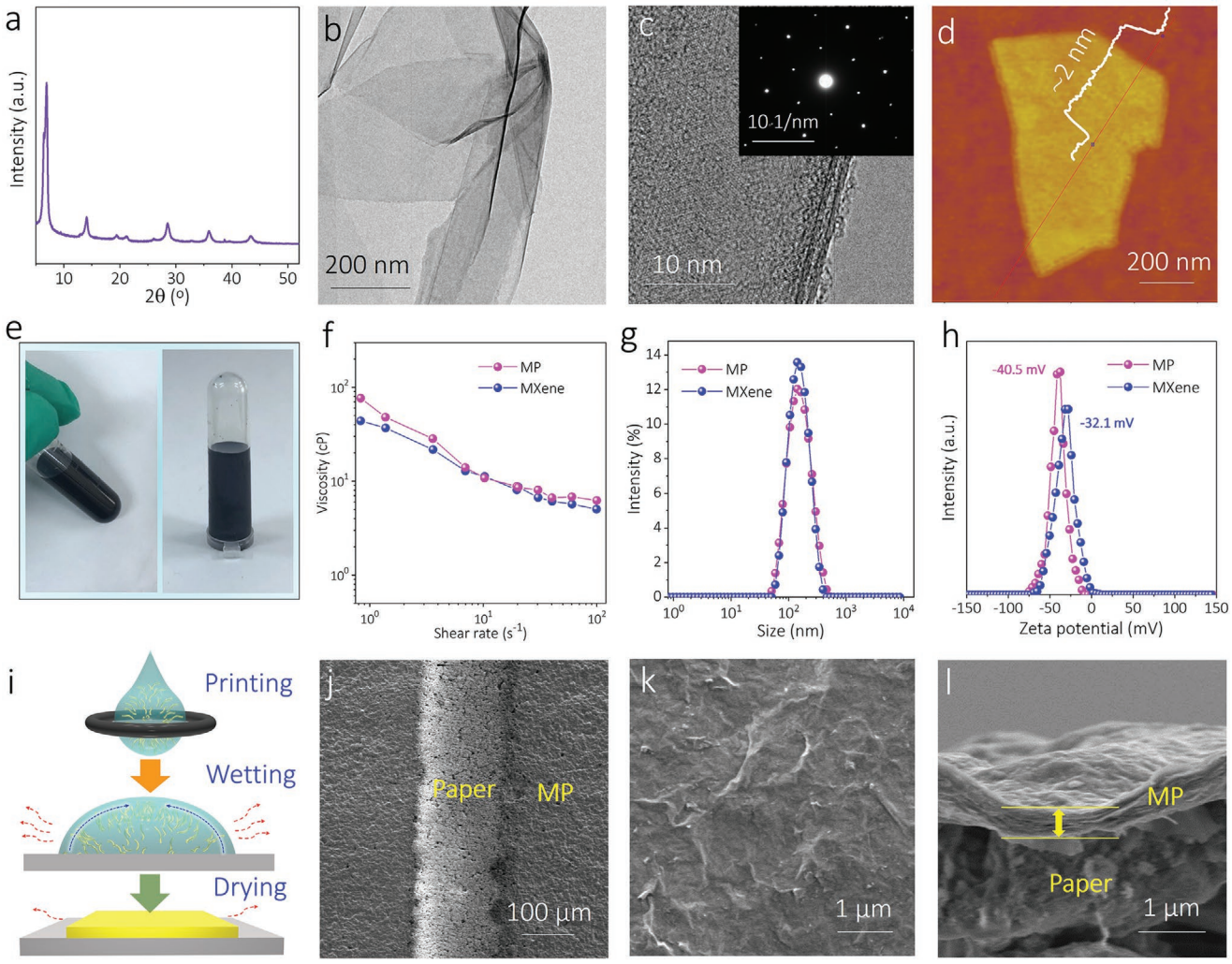

Figure 2. Characterization and properties of aqueous M ink and MP ink. a) X-ray diffraction (XRD) pattern, b) Transmission electron microscopy (TEM) image, and c) HRTEM image of MXene nanosheets. The inset in (c) is a selected-area electron diffraction image. d) Atomic force microscopy (AFM) image and corresponding height profile of MXene nanosheets. e) Digital photographs of MP ink in the normal and inverted states. f) Viscosity as a function of shear rate, g) size distribution, and h) zeta potential of M and MP inks. i) Schematic of inkjet-printing process of MP and M inks. j,k) Scanning electron microscopy (SEM) images of MP-MSC on photopaper with different magnifications. l) Cross-sectional SEM image of MP-MSCs-12.

with high stability was directly printed on various substrates to fabricate MSCs with customizable shapes (Figure 1a), e.g., interdigital and concentric-circle geometries. It should be noted that the PH1000 in the printed microelectrodes can effectively decrease the restacking of MXene layers and form conductive tunnels to facilitate charge transfer. In addition to MSCs for energy storage, the MP ink was also printed for the seamless integration of the TS current collector and the metal-free conductive circuits (Figure 1b). Subsequently, the thermosensitive ink was deposited by inkjet printing on the as-designed current collector for temperature monitoring. Finally, a Si film solar cell was serially connected with the printed MSC and TS to achieve the flexible, self-powered, integrated system.

2.2. Aqueous MXene Hybrid Inks for Inkjet Printing

The $Ti_3C_2T_x$ MXene was successfully synthesized by selectively etching the Ti_3AlC_2 phase with a LiF and HCl solution (**Figure 2**a).[37,38] The MXene nanosheets exhibited lateral dimension in the range of 0.2–1 µm (Figure 2b,d), ultrathin thickness of ≈2.3 nm (Figure 2c,d), and large interlayer space of 1.2 nm. A high concentration of aqueous MXene solution (≈30 mg mL^{-1}) was first prepared, followed by addition of glycol to decrease the viscosity and surface tension, resulting in aqueous pure MXene ink (denoted as M ink). On the other hand, aqueous MP hybrid ink was obtained by introducing 3.3 wt% of PH1000 into M ink for alleviating the restacking of MXene as well as constructing conductive channels (Figure 2e). During rheological property testing, both MP and M inks displayed shear-thinning behavior with increase of the shear rate, as shown in the viscosity-shear rate profiles (Figure 2f). The typical non-Newtonian character of the ink fluids enabled the successive jetting of the as-prepared inks during the printing process. In particular, the size distribution of both M and MP inks averaged ≈142 nm, avoiding nozzle clogging (Figure 2g). Moreover, due to the presence of the sulfonate groups of PH1000, the increased electrostatic repulsion between adjacent MXene nanosheets in MP ink resulted in a

lower zeta potential of –40.5 mV in contrast to M ink (–32.1 mV, Figure 2h). According to colloid theory, both MP and M inks exhibited electrostatically stable suspension (below –30 mV), which is crucial for printing.[39]

The printability of an ink is typically described by the Z value, the inverse of the Ohnesorge number (Oh), which can be calculated using the following Equation (1)[40]

$$Z = \frac{1}{Oh} = \frac{(\gamma\alpha\rho)^{1/2}}{\eta} \quad (1)$$

where γ is the surface tension, ρ is the density of the fluid, α is the inkjet nozzle diameter, and η is the dynamic viscosity. Normally, Z value of inks between 1 and 14 is regarded as suitable for inkjet printing.[41] According to the above equation, the Z values of M and MP inks are 2.19 and 1.81, respectively (Table S1, Supporting Information), suggesting that both can be stably jetted for printing. Additionally, during the process of printing, each droplet landed on the substrate as a fully round drop without trailing or formation of satellite droplets (Figure S1a and Video S1, Supporting Information). Thus, the printed droplets, lines, and films showed decent resolutions of 30, 90, and 160 μm on photopaper, respectively (Figure 2j; Figure S1b–d, Supporting Information).

When the jetting was completed, appropriate substrate wetting and ink drying dynamics played significant roles in the formation of uniform films. According to previous reports, the ideal substrate surface energy is supposed to be 7–10 mN m^{-1}, higher than the surface tension of inks.[42] It is noted that photopaper and resin-coated polyethylene terephthalate (PET) substrates with surface tension of ≈65 mN m^{-1} could be fully wetted by M and MP inks (58.6 mN m^{-1} for M ink, 55.6 mN m^{-1} for MP ink) (Figure S2, Supporting Information). During the evaporation of solvent from the MXene-based droplets, the water solvent would be evaporated first, and the existence of glycol weakened the Marangoni flow that would lead to the undesired coffee-ring effect (Figure 2i). Consequently, all printed MXene-based films or microelectrodes were of great uniformity without the coffee-ring effect (Figure S1c,d, Supporting Information), demonstrating exceptional stability and printability of aqueous M and MP inks. Also, the clear boundaries of the interdigital spaces can be easily distinguished between the microelectrodes of the MXene-based MSCs (Figure 2j; Figure S3a, Supporting Information). The aforementioned results indicate that an aqueous hybrid MP ink with suitable viscosity and well-matched surface tension was successfully achieved. The printed microelectrodes presented continuous MXene films and uniform elemental distribution (Figure 2k; Figure S3b–e and S4, Supporting Information), testifying to the outstanding coherence and uniformity of inkjet printing. In addition, the high-quality films in MP-MSCs with 12 printed layers of MP inks (MP-MSCs-12) and M-MSCs with five printed layers of M inks (M-MSCs-5) exhibited parallel-ordered structures with an average thickness of 25 nm per layer (Figure 2l; Figure S3c, Supporting Information), which was helpful for ion transport along the plane of MXene nanosheets.

Additionally, the printed microelectrodes exhibited excellent flexibility without any delamination from the substrate under bending and twisting, demonstrative of excellent structural integrity (Figure S5a, Supporting Information). It is noted that this mask-free inkjet printing technique was facile for implementing the modularized fabrication of MSCs (Figure S5b–d, Supporting Information) while enabling various programmed patterns (Figure 2m–q), paving a way for customizable geometries for microelectronics.

2.3. Electrochemical Performance of MP-MSCs

The electrochemical performance of M-MSCs and MP-MSCs was evaluated in H_2SO_4/polyvinyl alcohol (H_2SO_4/PVA) gel electrolyte by cyclic voltammetry (CV), galvanostatic charge–discharge (GCD), and electrochemical impedance spectroscopy (EIS). It was found that the area enclosed in the CV curves for MP-MSCs was obviously larger than that of M-MSCs (**Figure 3**a), implying a higher capacitance of MP-MSCs. Moreover, the CV curves for MP-MSCs-5 were rectangular, while M-MSCs-5 exhibited a shuttle shape (Figure S6a, Supporting Information), suggestive of facilitated ion-diffusion kinetics of the former. In addition, the voltage drop of MP-MSCs-5 was only 26 mV, lower than that of M-MSCs-5 (115 mV, Figures S6b and S7a, Supporting Information), implying improved electrical conductivity (Figure 3c). Specifically, MP-MSCs-5 showed a higher areal capacitance of 5.7 mF cm^{-2} than M-MSCs-5 with 2.6 mF cm^{-2} at 5 mV s^{-1}. Moreover, at a high scan rate (200 mV s^{-1}), MP-MSCs-5 achieved five times higher capacitance than M-MSCs-5, which corresponds to MP-MSCs offering a more robust capacitance retention of 52% compared to M-MSCs-5 (only 24%, Figure 3b). These extraordinary results of MP-MSCs compared to M-MSCs are mainly ascribed to the introduction of highly conductive PH1000 into the MP ink. In the printed MP microelectrodes, PH1000 as a small building block can not only effectively alleviate restacking between MXene nanosheets, leading to the exposure of more electrochemically active sites, but also simultaneously establish highly conductive channels for fast ion and electron transfer. This is further demonstrated by the EIS spectra and electrical conductivities of MP-MSCs and M-MSCs (Figure S8, Supporting Information). From the Bode plots, it is clear that the MP-MSCs show a higher characteristic frequency (0.31 Hz) than M-MSCs (0.21 Hz) at the phase angle of –45° (Figure S7b, Supporting Information), indicative of fast diffusion kinetics. Moreover, the microelectrode of the MP-MSCs had an improved electrical conductivity of 615 S cm^{-1}, which was superior to that of the M-MSCs (215 S cm^{-1}, Figure S7c, Supporting Information), further demonstrative of the synergy between MXene and PH1000.

High ion-electron conductivity in the high-areal-mass microelectrodes is one key parameter for boosting the areal/volumetric capacitances of MSCs; therefore, we further constructed MP-MSCs with different electrode thicknesses through repeated printing with 2, 5, 10, and 12 layers (Figure 3d) and examined the effect of thickness on the areal/volumetric capacitances as well as electrical conductivity of the microelectrodes. The equivalent series resistance (ESR) of MP-MSCs sharply decreased with the increment of the number of printed layers, owing to the improved conductivity (Figure S9a, Supporting Information). Specifically, MP-MSCs-12 exhibited the highest electrical conductivity of 700 S cm^{-1}

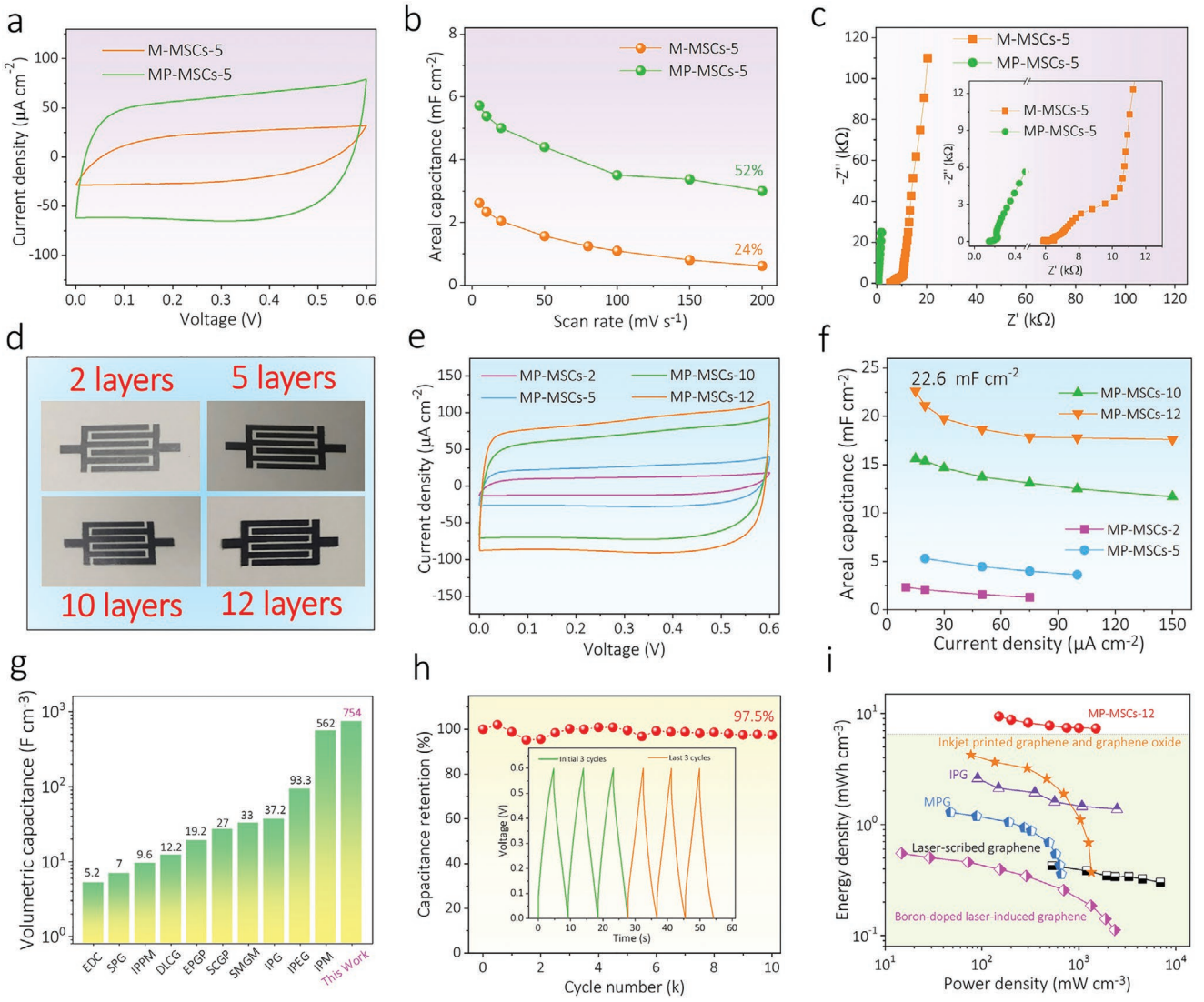

Figure 3. Electrochemical performance of M-MSCs and MP-MSCs measured in H_2SO_4/PVA gel electrolyte. a) CV curves at 50 mV s^{-1}, b) areal capacitance from 5 to 200 mV s^{-1}, and c) Nyquist plots of M-MSCs-5 and MP-MSCs-5. d) Digital photographs of MP-MSCs with different printed layers. e) CV curves at 20 mV s^{-1} and f) areal capacitance of MP-MSCs with different numbers of printed layers. g) Volumetric capacitance of MP-MSC-12 tested at 15 μA cm^{-2}, compared with previously reported MSCs. EDC: electrophoretic deposition carbon,[55] SPG: self-aligned printed graphene,[56] IPPM: inkjet-printed PEDOT/MnO_2,[44] DLSG: DVD laser-scribed graphene,[50] EPGP: extrusion-printed GO/PANi/PEDOT,[26] SCGP: spray-coated graphene/PEDOT,[54] SMGM: spray-masked graphene/MXene,[57] IPEG: inkjet-printed electrochemically exfoliated graphene,[46] IPM: inkjet-printed MXene.[35] h) Cycling stability of MP-MSCs-12 at 300 μA cm^{-2} for 10 000 cycles. Inset is GCD profiles of the first and last three cycles. i) Ragone plot of MP-MSCs-12 compared with previously reported MSCs.

(Figure S9b, Supporting Information). When the number of printed layers was increased, the current density of CV curves of all MP-MSCs increased (Figure 3e), suggesting an enlarged areal capacitance. Specifically, the areal capacitance was gradually improved from 2.3 mF cm^{-2} for MP-MSCs-2 to 22.6 mF cm^{-2} for MP-MSCs-12 (Figure 3f), which is much higher than those of previously reported printed MSCs (Figure S10c, Supporting Information), such as inkjet-printed MXene (12 mF cm^{-2})[35] and inkjet-printed graphene (2.8 mF cm^{-2}).[43] Taking into consideration the thickness of the microelectrode (300 nm for 12 layers), the volumetric capacitance of MP-MSCs-12 reached as high as ≈754 F cm^{-3} (Figure 3g), which is the highest value among inkjet-printed MSCs.[35,44–46] In addition, MP-MSCs-12 showed only a tiny capacitance decay with high capacitance retention of ≈78% for the scan rates from 20 to 150 mV s^{-1} (Figure 3f; Figure S10a, Supporting Information). More importantly, MP-MSCs-12 exhibited extraordinary cycling stability with 97.5% of its initial capacitance remaining after 10 000 continuous GCD cycles (Figure 3h). The Ragone plot of volumetric energy as a function of power density of MP-MSCs-12 and other reported MSCs is shown in Figure 3i. MP-MSCs-12 delivered an impressive energy density of 9.4 mWh cm^{-3} at a power density of 150 mW cm^{-3}, which is much higher than those of the previously reported MSCs (Table S3, Supporting

Information), such as inkjet-printed graphene and graphene oxide (4.33 mWh cm^{-3}),[47] inkjet-printed graphene (IPG, 2.6 mWh cm^{-3}),[46] methane-plasma-reduced graphene oxide (MPG, 1.29 mWh cm^{-3}),[48] boron-doped laser-induced graphene (0.55 mWh cm^{-3}),[49] and laser-scribed graphene (0.43 mWh cm^{-3}).[50]

To improve the working voltage and energy density, we employed the water-in-salt electrolyte with broad potential range to enlarge the voltage window of the MP-MSC, resulting from the decreased free water and suppressed hydrogen evolution reactions.[51,52] As shown in the linear-sweep voltammetry (LSV) curves (Figure S12, Supporting Information), the anodic and cathodic currents in highly concentrated 20 m (mol-salt in kg-solvent) LiCl electrolyte were observed at 1.2 and –1.5 V (vs Ag/AgCl), respectively, yielding a stable and large voltage range of 2.7 V. Under LiCl/SiO_2 gel electrolyte, the all-solid-state MP-MSCs-12 operated in the voltage range of 0–1.4 V (Figure S13a,b, Supporting Information). It is worth noting that MP-MSCs-12 delivered considerable areal capacitances of 8.8 and 6.0 mF cm^{-2} at 20 and 200 μA cm^{-2}, respectively (Figure S13c, Supporting Information), lower than that of MP-MSCs-12 in H_2SO_4/PVA electrolyte. However, the broad voltage range endowed MP-MSCs-12 with high energy density. The areal energy density and power density of MP-MSCs measured in LiCl/SiO_2 and H_2SO_4/PVA gel electrolyte were compared using a Ragone plot (Figure S14, Supporting Information). It was calculated that MP-MSCs-12 in LiCl/SiO_2 electrolyte (MP-MSCs-12(L)) delivered an excellent areal energy density of 0.56 μWh cm^{-2}, exceeding those of MP-MSCs-5(L) (0.36 μWh cm^{-2}), MP-MSCs-12 in H_2SO_4/PVA gel electrolyte (MP-MSCs-12(H), 0.28 μWh cm^{-2}), and MP-MSCs-5(H) (0.09 μWh cm^{-2}), respectively. Furthermore, the value is several orders of magnitude higher than those reported for printed MSCs, such as inkjet-printed graphene (0.0014 μWh cm^{-2}),[53] spray-coated graphene/PEDOT (0.089 μWh cm^{-2}),[54] and spray-coated graphene (0.028 μWh cm^{-2}).[54] Furthermore, the cycling stability of MP-MSCs-12 was demonstrated by 5000 continuous charge–discharge processes, exhibiting an extraordinary lifespan with 87.4% capacitance retention (Figure S13d, Supporting Information).

2.4. Shape Customization and Flexibility of MP-MSCs

To highlight the customizability of MP-MSCs, we constructed variform MP-MSCs connected in series and in parallel, such as ones with a strip shape (inset of **Figure 4**b) or concentric circles (inset of Figure 4d). Notably, the highly conductive MP inks with excellent rheological behavior enable the printed patterns to simultaneously serve as microelectrodes and metal-free interconnects. As shown in the CV curves and GCD profiles (Figure 4a,b), the total current output and discharge time of integrated MP-MSCs increased in proportion by increasing the number of the parallel-connected cells, resulting in a linear increase of capacitance (Figure 4c). Meanwhile, the concentric-circle MP-MSCs connected in series exhibited a stepwise voltage increase from 0.6 V for a single cell to 1.8 V for three cells. Also, the current in the CV curves decreased accordingly, while the discharge time in the GCD profiles was unchanged (Figure 4d,e), accompanied by the enlargement of ESR from 0.71 to 3.33 kΩ (Figure S15, Supporting Information). These results strongly reveal the shape diversity, excellent performance uniformity, and performance tunability of inkjet-printed devices. Furthermore, the high-precision inkjet printing technique can achieve a high areal-number density of MP-MSCs (9 cells cm^{-2}), delivering a decent voltage density of 5.4 V cm^{-2} (Figure 4f; Figure S16, Supporting Information), thus indicative of high precision and architectural uniformity. Additionally, 60 serially connected MP-MSCs free of metal-based interconnects delivered an ultrahigh voltage output of 36 V, demonstrative of superior modularization (Figure 4g). Due to the highly conductive MP ink and versatile printing technique, the integrated MSCs could be mass produced with tailored voltage and capacitance in a limited area to satisfy the various demands of specific microelectronic applications. As an example, it was clearly obseved that all the CV curves of concentric-circle MP-MSCs at different bending angles from 0° to 180° nearly completely overlapped (Figure 4h), implying outstanding structural stability and mechanical flexibility. Furthermore, three serially connected concentric-circle MP-MSCs in the flat and bent states could directly serve as standalone microscale power sources to light a liquid crystal display (LCD) showing "2D Materials & Energy Devices" (Figure 4e; Figure S17, Supporting Information), indicative of the practicality of MP-MSCs for flexible microelectronics.

2.5. Self-Powered Integrated System

To further demonstrate the superiority of aqueous MP hybrid inks, a prototype of flexible, self-powered, integrated system was fabricated (**Figure 5**a,b; Figure S18, Supporting Information). First, a flexible Si film solar cell was deposited on a stainless-steel substrate via plasma-enhanced chemical vapor deposition (PECVD). Subsequently, the MP ink was printed on a resin-coated PET substrate as the energy storage unit, followed by the current collector of the TS and metal-free conductive circuits. Finally, the thermosensitive ink was precisely printed on the aforementioned MP current collectors and gel electrolyte was coated onto the microelectrodes of the MP-MSC. Impressively, the Si solar cell showed an open-circuit voltage of ≈0.67 V with a short-circuit current density of 20 mA cm^{-2} (Figure 5c), which was enough to charge a MP-MSC. When photo-charged by the solar cell, the MP-MSC showed a normal galvanostatic discharge process at various current densities from 10 to 100 μA cm^{-2} (Figure 5d). Notably, the charged MP-MSC exhibited a low self-discharge rate with a stable voltage of 0.34 V for 1 h and 0.25 V for 10 h, respectively (Figure S19, Supporting Information), validating the sustained power supply for energy consumption.

This flexible, self-powered, integrated system relied on the Si solar cell as the energy harvester and the MP-MSC for power storage. The TS displayed a steady response under infrared irradiation by a grill light, resulting in decreased current (current is inversely proportional to temperature) (Figure 5e). The plot shows that the current response linearly increased as the applied temperature rose, from which the highest response value of the self-powered TS reached ≈2.0% at 50 °C (Figure 5f). Remarkably, once the MP-MSC was photo-charged, it could power the printed sensor with continuous, long-duration and reversible response of ≈1.0% under periodic heating to 40 °C for

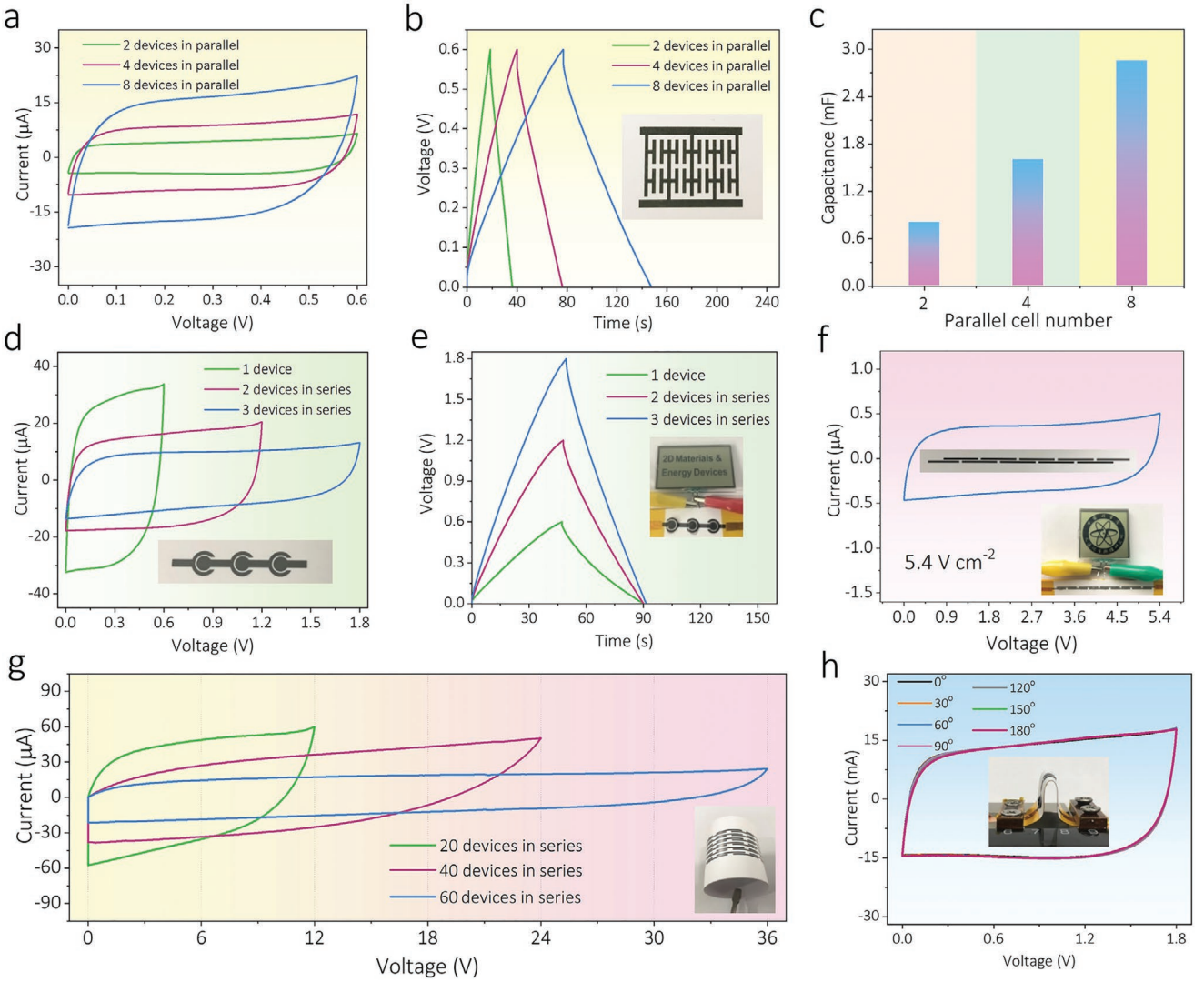

Figure 4. Integration and flexibility of MP-MSCs. a) CV curves at 20 mV s^{-1}, b) GCD profiles at current of 6.5 μA, and c) capacitance at 6.5 μA of strip-shaped MP-MSCs with different numbers of parallel devices. Inset in (b) is a digital photograph of eight parallelly connected strip-shaped MP-MSCs. d) CV curves at 50 mV s^{-1} and e) GCD profiles at 5.8 μA of concentric-circle MP-MSCs with different numbers of devices in series from 1 to 3. Insets in (d) and (e) are digital photographs of concentric-circle MP-MSCs and an LCD displaying "2D Materials & Energy Devices," respectively. f) CV curve of nine serially connected linear MP-MSCs with the area of 1 cm^2. The inset shows digital photographs of the device alone and powering an LCD displaying the DICP logo. g) CV curves of 20, 40, and 60 tandem cells tested at a scan rate of 100 mV s^{-1}. h) CV curves tested at various bending states, e.g., 30°, 60°, 90°, 120°, and 180°. Inset is a photograph of MP-MSCs bent at 180°.

5 cycles (Figure 5g; Figure S20, Supporting Information), clearly indicative of excellent sensing reliability. Furthermore, the planar, self-powered sensor system exhibited mechanical durability, delivering a good response retention of over 95% even at a high bending angle of 180°, demonstrative of exceptional flexibility and stability of the inkjet-printed integrated MSC and sensor (Figure 5h; Figure S21, Supporting Information). These results testify that the self-powered integrated system can serve as an independent unit in future smart and flexible wearable systems.

3. Conclusion

We demonstrate an aqueous MP hybrid ink suitable for inkjet printing of high-performance MSCs on various flexible substrates, through the synergy of ultrahigh capacitance MXene and highly conductive PH1000 by preventing MXene's restacking in the highly ion-electron-conducting microelectrodes. The customized microelectrodes could be manufactured within seconds by simple parameter adjustments, which rendered shape diverse MSCs with high resolution and landmark volumetric capacitance of 754 F cm^{-3}. Such characteristics are cornerstones for the development of powerful miniaturized flexible MSCs that can be easily integrated with microelectronics. We showcase this possibility by printing the microelectrodes of the MSC, sensor, and the interconnects between them in a single printing step. Connected to a flexible solar cell, the self-powered integrated microsystem monitored temperature repeatedly with excellent response of 2% and displayed robust mechanical resilience under various bending tests. Such rationally designed methods from synergistic hybrid

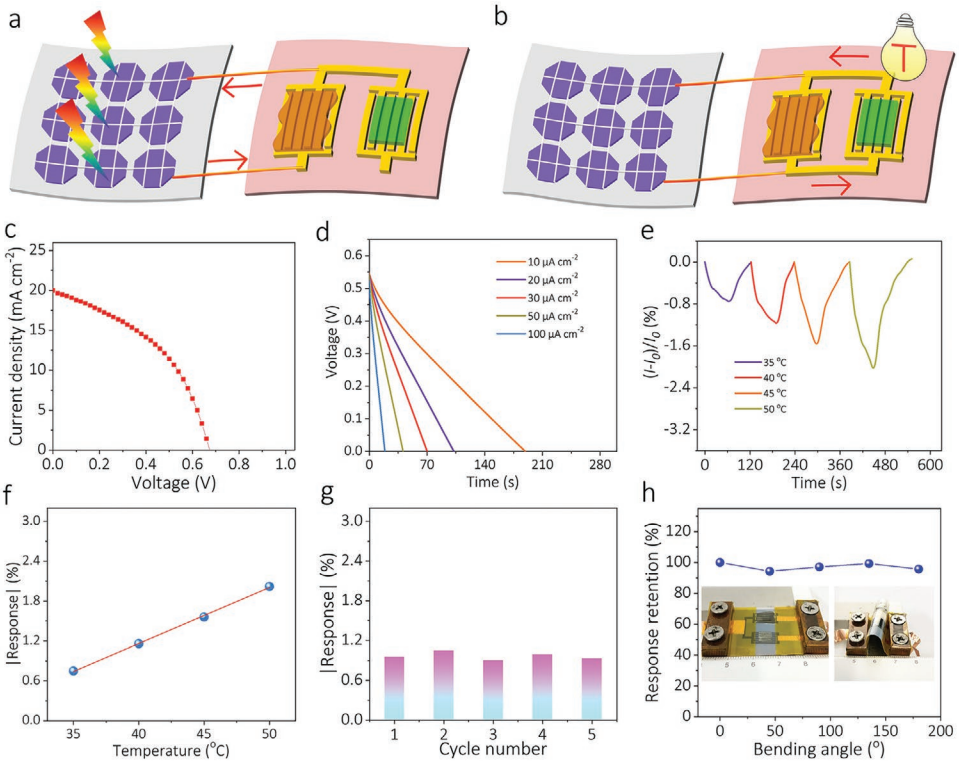

Figure 5. The self-powered integrated system for temperature monitor. a) Schematic illustration of the charging process of the MP-MSC by the Si film solar cell. b) Schematic of the self-powered integrated sensor under the irradiation of an infrared grill light. c) Current–voltage curve of the flexible Si film solar cell on the stainless steel substrate. d) Discharge curves of MP-MSCs charged by the solar cell for 30 s. e) Current change curves and f) corresponding response value of the self-powered temperature sensor under the temperature range of 35–50 °C. g) Response of self-powered temperature sensor for 5 cycles. h) Response ratio of the self-powered temperature sensor as a function of bending angle. Insets are photographs of the planar MSC-sensor integrated system in the flat and bending states.

ink synthesis to multi-scale device assembly can reduce the production cost and environmental footprint while increasing the production rate and assembly efficiency. This strategy will accelerate the development of printable inks as easy-to-intergrate, self-sustained components tailorable for next-generation, self-powered, wearable, and implantable microelectronics.

Supporting Information

Supporting Information is available from the Wiley Online Library or from the author.

Acknowledgements

J.M. and S.Z. contributed equally to this work. This work was financially supported by the National Key R&D Program of China (grant 2016YFA0200200), the National Natural Science Foundation of China (grant nos. 22075279, 51872283, 21805273, 51622210, 51872277, 22005297, 22005298), the Central Government of Liaoning Province Guided the Funds for Local Science and Technology Development (grant 2021JH6/10500112), the Strategic Priority Research Program of Chinese Academy of Sciences (grant no. XDA17040506), Dalian Innovation Support Plan for High Level Talents (2019RT09), Dalian National Laboratory For Clean Energy (DNL), CAS, DNL Cooperation Fund, CAS (DNL180310, DNL180308, DNL201912, and DNL201915), the Liao Ning Revitalization Talents Program (grant XLYC1807153), theNatural Science Foundation of Liaoning Province, Joint Research Fund Liaoning-Shenyang National Laboratory for Materials Science (grant 20180510038), DICP (DICP ZZBS201708, DICP ZZBS201802, and DICP I2020032), and DICP&QIBEBT (grant DICP&QIBEBT UN201702).

Conflict of Interest

The authors declare no conflict of interest.

Data Availability Statement

Research data are not shared.

Keywords

inkjet printing, micro-supercapacitors, MXene ink, printable temperature sensors, self-powered integrated systems

Received: March 4, 2021
Revised: March 25, 2021
Published online: April 28, 2021

[1] B. D. Gates, *Science* **2009**, *323*, 1566.
[2] Z. Wen, M.-H. Yeh, H. Guo, J. Wang, Y. Zi, W. Xu, J. Deng, L. Zhu, X. Wang, C. Hu, L. Zhu, X. Sun, Z. L. Wang, *Sci. Adv.* **2016**, *2*, e1600097.

[3] J. Xu, Y. Chen, L. Dai, *Nat. Commun.* **2015**, *6*, 8013.
[4] S. Xu, Y. Qin, C. Xu, Y. Wei, R. Yang, Z. L. Wang, *Nat. Nanotechnol.* **2010**, *5*, 366.
[5] S. A. Hashemi, S. Ramakrishna, A. G. Aberle, *Energy Environ. Sci.* **2020**, *13*, 685.
[6] P. Zhang, F. Wang, M. Yu, X. Zhuang, X. Feng, *Chem. Soc. Rev.* **2018**, *47*, 7426.
[7] H. Wu, L. Xu, Y. Wang, T. Zhang, H. Zhang, C. R. Bowen, Z. L. Wang, Y. Yang, *ACS Energy Lett.* **2020**, *5*, 3708.
[8] J. Ma, S. Zheng, P. Das, P. Lu, Y. Yu, Z.-S. Wu, *Small Struct.* **2020**, *1*, 2000053.
[9] J. Chen, Z. L. Wang, *Joule* **2017**, *1*, 480.
[10] S. Zheng, X. Shi, P. Das, Z. S. Wu, X. Bao, *Adv. Mater.* **2019**, *31*, 1900583.
[11] Y. Lin, J. Chen, M. M. Tavakoli, Y. Gao, Y. Zhu, D. Zhang, M. Kam, Z. He, Z. Fan, *Adv. Mater.* **2018**, *31*, 1804285.
[12] Y. Huang, M. Zhu, Y. Huang, Z. Pei, H. Li, Z. Wang, Q. Xue, C. Zhi, *Adv. Mater.* **2016**, *28*, 8344.
[13] S. Zheng, H. Wang, P. Das, Y. Zhang, Y. Cao, J. Ma, S. F. Liu, Z. S. Wu, *Adv. Mater.* **2021**, *33*, 2005449.
[14] S. Qin, Q. Zhang, X. Yang, M. Liu, Q. Sun, Z. L. Wang, *Adv. Energy Mater.* **2018**, *8*, 1800069.
[15] J. Yun, C. Song, H. Lee, H. Park, Y. R. Jeong, J. W. Kim, S. W. Jin, S. Y. Oh, L. Sun, G. Zi, J. S. Ha, *Nano Energy* **2018**, *49*, 644.
[16] M. F. El-Kady, M. Ihns, M. Li, J. Y. Hwang, M. F. Mousavi, L. Chaney, A. T. Lech, R. B. Kaner, *Proc. Natl. Acad. Sci. USA* **2015**, *112*, 4233.
[17] M. Beidaghi, Y. Gogotsi, *Energy Environ. Sci.* **2014**, *7*, 867.
[18] X. Shi, S. Pei, F. Zhou, W. Ren, H.-M. Cheng, Z.-S. Wu, X. Bao, *Energy Environ. Sci.* **2019**, *12*, 1534.
[19] S. Zheng, X. Tang, Z. S. Wu, Y. Z. Tan, S. Wang, C. Sun, H. M. Cheng, X. Bao, *ACS Nano* **2017**, *11*, 2171.
[20] X. Shi, Z. S. Wu, J. Qin, S. Zheng, S. Wang, F. Zhou, C. Sun, X. Bao, *Adv. Mater.* **2017**, *29*, 1703034.
[21] X. Wang, S. Zheng, F. Zhou, J. Qin, X. Shi, S. Wang, C. Sun, X. Bao, Z.-S. Wu, *Natl. Sci. Rev.* **2020**, *7*, 64.
[22] K.-H. Choi, J. Yoo, C. K. Lee, S.-Y. Lee, *Energy Environ. Sci.* **2016**, *9*, 2812.
[23] K.-H. Choi, D. B. Ahn, S.-Y. Lee, *ACS Energy Lett.* **2017**, *3*, 220.
[24] H. Li, J. Liang, *Adv. Mater.* **2019**, *32*, 1805864.
[25] Y. Lin, Y. Gao, Z. Fan, *Adv. Mater.* **2019**, *29*, 1701736.
[26] Y. Liu, B. Zhang, Q. Xu, Y. Hou, S. Seyedin, S. Qin, G. G. Wallace, S. Beirne, J. M. Razal, J. Chen, *Adv. Funct. Mater.* **2018**, *28*, 1706592.
[27] M. R. Lukatskaya, S. Kota, Z. Lin, M.-Q. Zhao, N. Shpigel, M. D. Levi, J. Halim, P.-L. Taberna, M. W. Barsoum, P. Simon, Y. Gogotsi, *Nat. Energy* **2017**, *2*, 17105.
[28] C. Zhang, M. P. Kremer, A. Seral-Ascaso, S.-H. Park, N. McEvoy, B. Anasori, Y. Gogotsi, V. Nicolosi, *Adv. Funct. Mater.* **2018**, *28*, 1705506.
[29] L. Huang, X. Gu, G. Zheng, *Chem* **2019**, *5*, 15.
[30] J. L. Hart, K. Hantanasirisakul, A. C. Lang, B. Anasori, D. Pinto, Y. Pivak, J. T. van Omme, S. J. May, Y. Gogotsi, M. L. Taheri, *Nat. Commun.* **2019**, *10*, 522.
[31] D. B. Ahn, S.-S. Lee, K.-H. Lee, J.-H. Kim, J.-W. Lee, S.-Y. Lee, *Energy Storage Mater.* **2020**, *29*, 92.
[32] S. Liu, J. Li, X. Yan, Q. Su, Y. Lu, J. Qiu, Z. Wang, X. Lin, J. Huang, R. Liu, B. Zheng, L. Chen, R. Fu, D. Wu, *Adv. Mater.* **2018**, *30*, 1706895.
[33] Q. Jiang, Y. Lei, H. Liang, K. Xi, C. Xia, H. N. Alshareef, *Energy Storage Mater.* **2020**, *27*, 78.
[34] M. Vural, A. Pena-Francesch, J. Bars-Pomes, H. Jung, H. Gudapati, C. B. Hatter, B. D. Allen, B. Anasori, I. T. Ozbolat, Y. Gogotsi, M. C. Demirel, *Adv. Funct. Mater.* **2018**, *28*, 1801972.
[35] C. J. Zhang, L. McKeon, M. P. Kremer, S. H. Park, O. Ronan, A. Seral-Ascaso, S. Barwich, C. O. Coileain, N. McEvoy, H. C. Nerl, B. Anasori, J. N. Coleman, Y. Gogotsi, V. Nicolosi, *Nat. Commun.* **2019**, *10*, 1795.
[36] N. Kim, S. Kee, S. H. Lee, B. H. Lee, Y. H. Kahng, Y. R. Jo, B. J. Kim, K. Lee, *Adv. Mater.* **2014**, *26*, 2268.
[37] F. Shahzad, M. Alhabeb, C. B. Hatter, B. Anasori, S. M. Hong, C. M. Koo, Y. Gogotsi, *Science* **2016**, *353*, 1137.
[38] Y. Xia, T. S. Mathis, M. Q. Zhao, B. Anasori, A. Dang, Z. Zhou, H. Cho, Y. Gogotsi, S. Yang, *Nature* **2018**, *557*, 409.
[39] K.-H. Lee, S.-S. Lee, D. B. Ahn, J. Lee, D. Byun, S.-Y. Lee, *Sci. Adv.* **2020**, *6*, eaaz1692.
[40] G. Hu, J. Kang, L. W. T. Ng, X. Zhu, R. C. T. Howe, C. G. Jones, M. C. Hersam, T. Hasan, *Chem. Soc. Rev.* **2018**, *47*, 3265.
[41] L. J. Deiner, T. L. Reitz, *Adv. Eng. Mater.* **2017**, *19*, 1600878.
[42] G. Hu, T. Albrow-Owen, X. Jin, A. Ali, Y. Hu, R. C. T. Howe, K. Shehzad, Z. Yang, X. Zhu, R. I. Woodward, T. C. Wu, H. Jussila, J. B. Wu, P. Peng, P. H. Tan, Z. Sun, E. J. R. Kelleher, M. Zhang, Y. Xu, T. Hasan, *Nat. Commun.* **2017**, *8*, 278.
[43] R. Fang, S. Zhao, Z. Sun, D.-W. Wang, H.-M. Cheng, F. Li, *Adv. Mater.* **2017**, *29*, 1606823.
[44] Y. Wang, Y.-Z. Zhang, D. Dubbink, J. E. t. Elshof, *Nano Energy* **2018**, *49*, 481.
[45] L. Li, E. B. Secor, K.-S. Chen, J. Zhu, X. Liu, T. Z. Gao, J.-W. T. Seo, Y. Zhao, M. C. Hersam, *Adv. Energy Mater.* **2016**, *6*, 1600909.
[46] J. Li, S. Sollami Delekta, P. Zhang, S. Yang, M. R. Lohe, X. Zhuang, X. Feng, M. Ostling, *ACS Nano* **2017**, *11*, 8249.
[47] S. Sollami Delekta, K. H. Adolfsson, N. Benyahia Erdal, M. Hakkarainen, M. Ostling, J. Li, *Nanoscale* **2019**, *11*, 10172.
[48] Z. S. Wu, K. Parvez, X. Feng, K. Mullen, *Nat. Commun.* **2013**, *4*, 2487.
[49] Z. Peng, R. Ye, J. A. Mann, D. Zakhidov, Y. Li, P. R. Smalley, J. Lin, J. M. Tour, *ACS Nano* **2015**, *9*, 5868.
[50] M. F. El-Kady, R. B. Kaner, *Nat. Commun.* **2013**, *4*, 1475.
[51] L. Suo, O. Borodin, W. Sun, X. Fan, C. Yang, F. Wang, T. Gao, Z. Ma, M. Schroeder, A. von Cresce, S. M. Russell, M. Armand, A. Angell, K. Xu, C. Wang, *Angew. Chem., Int. Ed.* **2016**, *55*, 7136.
[52] C. Yang, J. Chen, X. Ji, T. P. Pollard, X. Lu, C. J. Sun, S. Hou, Q. Liu, C. Liu, T. Qing, Y. Wang, O. Borodin, Y. Ren, K. Xu, C. Wang, *Nature* **2019**, *569*, 245.
[53] S. Sollami Delekta, A. D. Smith, J. Li, M. Ostling, *Nanoscale* **2017**, *9*, 6998.
[54] Z. Liu, Z. S. Wu, S. Yang, R. Dong, X. Feng, K. Mullen, *Adv. Mater.* **2016**, *28*, 2217.
[55] D. Pech, M. Brunet, H. Durou, P. Huang, V. Mochalin, Y. Gogotsi, P. L. Taberna, P. Simon, *Nat. Nanotechnol.* **2010**, *5*, 651.
[56] W. J. Hyun, E. B. Secor, C.-H. Kim, M. C. Hersam, L. F. Francis, C. D. Frisbie, *Adv. Energy Mater.* **2017**, *7*, 1700285.
[57] H. Li, Y. Hou, F. Wang, M. R. Lohe, X. Zhuang, L. Niu, X. Feng, *Adv. Energy Mater.* **2017**, *7*, 1601847.